Journal of Colloid and Interface Science 652 (2023) 1974–1983

Contents lists available at ScienceDirect

Journal of Colloid And Interface Science

journal homepage: www.elsevier.com/locate/jcis

Effects of particle shape and surface roughness on van der Waals interactions and coupling to dynamics in nanocrystals

Jaewon Lee [a,*], Elias Nakouzi [b], Jaeyoung Heo [b], Benjamin A. Legg [b], Gregory K. Schenter [b], Dongsheng Li [b], Chanwoo Park [a], Hongbin Ma [a], Jaehun Chun [b,c,*]

[a] Department of Mechanical and Aerospace Engineering, University of Missouri, 416 South 6th Street, Columbia 65211, United States
[b] Physical and Computational Sciences Directorate, Pacific Northwest National Laboratory, Richland, Washington 99352, United States
[c] Levich Institute and Department of Chemical Engineering, CUNY City College of New York, New York, New York 10031, United States

GRAPHICAL ABSTRACT

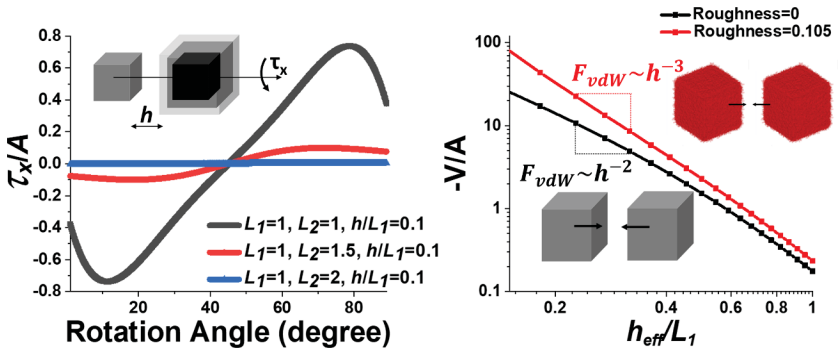

ARTICLE INFO

Keywords:
van der Waals forces/torques
Self-assembly
Particle shape
Surface roughness
Arbitrary configurations
Scaling

ABSTRACT

The van der Waals interaction between colloids and nanoparticles is one of the key components to understanding particle aggregation, attachment, and assembly. While the ubiquity of anisotropic particle shapes and surface roughness is well-recognized in nanocrystalline materials, the effects of both on van der Waals forces and torques have not been adequately investigated. In this study, we develop a numerical scheme to determine the van der Waals forces and torques between cubic particles with multiple configurations and relative orientations. Our results show that the van der Waals torque due to anisotropic particle shapes is appreciable at nearly all configurations and mutual angles, outcompeting Brownian torque for various materials systems and conditions. Surface roughness enhances this particle shape effect, resulting in stronger van der Waals interactions ascribed to protrusions on the surfaces. Moreover, a scaling analysis indicates that the surface roughness alters the separation dependence of the van der Waals force and, more importantly, significantly influences the dynamics of two approaching particles. Our results clearly demonstrate that surface roughness and anisotropic shape play a

Abbreviations: vdW, van der Waals; A, Hamaker constant; RMS, root-mean-square roughness; V_{vdW}, van der Waals potential.; F_{vdW}, van der Waals force.; τ_{vdW}, van der Waals torque.; h, separation distance.; M, hydrodynamic mobility.; ε, normalized separation scaled by the radius of a spherical particle or a half-length of a cubic particle.

* Corresponding authors at: Department of Mechanical and Aerospace Engineering, University of Missouri, 416 South 6th Street, Columbia 65211, United States (J. Lee). Physical and Computational Sciences Directorate, Pacific Northwest National Laboratory, Richland, Washington 99352, United States (J. Chun).
E-mail addresses: j.lee@missouri.edu (J. Lee), Jaehun.Chun@pnnl.gov (J. Chun).

https://doi.org/10.1016/j.jcis.2023.08.160
Received 17 April 2023; Received in revised form 22 August 2023; Accepted 25 August 2023
Available online 26 August 2023

crucial role in the energetics and kinetics of various particle-scale and emergent phenomena, such as crystal growth by oriented attachment, nanomaterials synthesis and assembly, mud flow rheology, as well as the deposition of natural nanocrystals within the subsurface.

1. Introduction

Colloids and nanoparticles in solutions can aggregate, attach, assemble, or remain dispersed due to a balance of interparticle forces. These outcomes depend on a multitude of variables including material chemistry, solution conditions, surface charge, and particle geometry. Most commonly, the stability of colloidal systems is evaluated using the Derjaguin-Landau-Verwey-Overbeek (DLVO) theory, which accounts for contributions from the electrostatic force and the van der Waals force. While the DLVO theory has demonstrated relative success for predicting the aggregation rates of spherical colloids, many significant limitations persist. For instance, continuum approximations do not accurately describe the molecular nature of the solution medium, [1] non-DLVO interactions such as hydration forces are not fully understood, [2] and real-world complexities such as non-spherical particle shapes and surface roughness remain difficult to characterize. In particular, incorporating particle geometry in force calculations will require advanced numerical schemes capable of applying existing theory to random shapes and roughness, beyond exemplary smooth spheres. Resolving these complexities promises a more predictive theory that advances a wide range of application areas including environmental remediation, nanomaterials synthesis, manufacturing, cosmetics and other industries, as well as nuclear waste treatment. [3–5].

In particular, the ubiquitous van der Waals (vdW) interaction, also known as the London-vdW or dispersion interaction, is a key component of the DLVO theory, especially critical for understanding various physicochemical phenomena beyond the traditional view of colloidal aggregation. [6,7] For example, Lee et al. showed that the vdW force is the main driver for the assembly of Ag nanoparticles into a superlattice structure and that a delicate balance between hydration and vdW forces results in a distinct distribution of interparticle separations. [2,8] Similarly, a superlattice pattern of Pt-Fe nanoparticles emerges when vdW interactions dominate at shorter particle separations after long-range anisotropic forces initially drive the formation of chain-like patterns. [9] The manipulation of these interparticle forces has enabled the synthesis of an impressive repertoire of nanomaterials, including the reversible formation of Janus metal-organosilica nanoparticles, [10] the assembly of highly-ordered "mesocrystals" [11] and nanorod chains [12], and the oriented attachment of nanocrystals that subsequently fuse into single crystals. [13] Furthermore, the vdW force at the particle scale can influence emergent phenomena at the macroscopic scale such as the mechanical response and rheology of nanoparticle dispersions. [14,15] Recent studies demonstrated that an attractive force between particles such as vdW force is responsible for the cohesive nature of dense suspensions that mitigate the expected shear thickening. That is, as the magnitude of vdW forces increases, the viscosity of dense suspensions increases with shear at a smaller shear rate (or smaller Péclet number), obscuring the expected shear thickening at higher shear rates. [15,16].

While many previous studies have aimed to understand the vdW interaction and its consequences at macroscopic scales for colloids and nanoparticle systems, [17–20] these cannot be directly applicable to nanocrystals because of two key unique features: inherent surface roughness and non-spherical shapes of faceted crystals with sharp edges. Attempts at resolving the effect of particle shapes have largely focused on scaling arguments using very specific configurations such as direct face-face interaction between faceted particles. One such example showed that the interplay of vdW force and hydrodynamic mobility in rhombohedral boehmite nanocrystals results in unexpected particle packing and aggregation dynamics. [21] This result demonstrates that the correlation between energetics and dynamics for anisotropic particles is markedly different than for colloidal spheres, [4,7] leading to a richness of emergent behavior. [21] Krzysko et al. further demonstrated that such coupling can also lead to a viscosity increase of boehmite nanocrystal suspensions under shear in a study using a combination of capillary rheometry and in situ (ultra) small angle X-ray scattering. [17,22] One of the key next steps will be developing a quantitative understanding to implement "vdW torque" between non-spherical particles, beyond simple scaling arguments.

In addition to shape complexities, nanocrystals inherently possess "microscopic" surface roughness associated with defects, step-edges, and foreign adsorbates. In principle, these features can be expected to produce variations in the separation between two bodies, leading to a noticeable change in vdW interactions. Delrio et al. used adhesion force measurements and simulations to show that vdW forces between micromachined surfaces are greatly influenced by surface roughness. [23] Parsons et al. showed that the surface roughness generally amplifies the long-range behavior of noncontact electrostatic/vdW forces between two surfaces based on a simple model implementing the Derjaguin approximation with root-mean-square roughness as a key parameter and experimental force measurements on TiO_2 surfaces. [24] However, such studies have been largely based on two semi-infinite flat surfaces such that the effect of finite particle size and, more importantly, the connection of the vdW force to the non-spherical shapes and relative particle orientations remain unresolved.

In this work, we investigated the effect of shape and surface roughness on the vdW interaction between nanocrystals using two cubic particles as a model system. Our results reveal mechanistic insights into vdW interactions between nanocrystals, especially connecting to the orientation dependence of the vdW interaction, with particular emphasis on vdW torque, and corresponding translational/rotational dynamics of nanocrystals in the context of assembly and aggregation. It is noteworthy that various previous studies for vdW torque have been mainly focused on vdW torque from its crystallographic nature that requires a full frequency-dependent dielectric function of each crystallographic direction, not necessarily coupled to the shape [25–27]; we aim here to clearly quantify the vdW torque from an orientation-dependent vdW interactions due to an anisotropic shape irrespective of crystallographic nature. Hereafter, we will briefly explain the scheme to numerically construct nanocrystals and surface roughness, as well as the basic formulation to calculate the vdW interaction and corresponding force/torque.

2. Basic theoretical formulations and simulation schemes

2.1. Formulation for vdW interaction and force/torque between two cubes

The London-vdW interaction energy between two macroscopic bodies can be described as

$$V = -\left(A/\pi^2\right)V_R \tag{1}$$

where A is the Hamaker constant depending on dielectric properties of the bodies and intervening medium. V_R represents geometric effects of two macroscopic bodies. Utilizing Hamaker's approach[28]:

$$V_R = \int_{v_1}\int_{v_2} \frac{1}{|\mathbf{r}_1 - \mathbf{r}_2|^6} d\mathbf{r}_1 d\mathbf{r}_2 \tag{2}$$

where $r = |\mathbf{r}_1\text{-}\mathbf{r}_2|$ is the distance between an arbitrary point in Body 1 (volume v_1) and an arbitrary point in Body 2 (volume v_2). Our approach for calculating V_R of cubes in arbitrary configurations is a numerical summation of the discretized small pieces, each intended to represent a

group of atoms.

$$V_R = \sum_n \sum_m \sum_p V_{R-nmp} \tag{3}$$

where $V_{R\text{-}nmp}$ indicates the geometric effect of vdW interaction between a Body 1 and each small piece of a Body 2. As shown in Fig. 1, given geometrical parameters (i.e., dimensions of length, thickness, and width of Body 1: $2L_1$, $2\ T_1$, $2\ W_1$; dimensions of length, thickness, and width of Body 2: $2L_2$, $2\ T_2$, $2\ W_2$; x-, y-, and z-directional separation distance: hx, hy, and hz), the center positions of the small pieces in the Body 2 can be calculated based on the center position (x_{body2}, y_{body2}, and z_{body2}).

$$\begin{aligned}(x_{c\_i}, y_{c\_j}, z_{c\_k}) = \big(&x_{body2} - L_2 + (2L_2/n) \bullet (N - 0.5), y_{body2} - T_2 + (2T_2/m) \\ &\bullet (M - 0.5), z_{body2} - W_2 + (2W_2/p) \bullet (P - 0.5)\big)\end{aligned} \tag{4}$$

where n, m and p are the number of slices in x, y, and z coordinates, respectively. N, M and P are the integer from 1 to n, m or p to define the center position of the sliced small pieces in the Body 2. In this work, a 10 × 10 × 10 grid has been used. That is, 2 (dimensionless unit) of each side was used for $2L_2$, $2\ T_2$, and $2\ W_2$ dimensions (i.e., cube), and 0.2 was used for $2L_2/n$, $2\ T_2/m$, and $2\ W_2/p$ by $n = 10$, $m = 10$, and $p = 10$. The center positions of the sliced small pieces in the Body 2 were rotated by using the rotation matrix based on the rotation angle θ_x, θ_y and θ_z with respect to x-axis, y-axis, and z-axis respectively:[29]

$$\begin{pmatrix} x'_{c4} \\ y'_{c4} \\ z'_{c4} \end{pmatrix} = \begin{pmatrix} cos\theta_x & -sin\theta_x & 0 \\ sin\theta_x & cos\theta_x & 0 \\ 0 & 0 & 1 \end{pmatrix} \begin{pmatrix} cos\theta_y & 0 & sin\theta_y \\ 0 & 1 & 0 \\ -sin\theta_y & 0 & cos\theta_y \end{pmatrix} \begin{pmatrix} 1 & 0 & 0 \\ 0 & cos\theta_z & -sin\theta_z \\ 0 & sin\theta_z & cos\theta_z \end{pmatrix} \begin{pmatrix} x_{c4} \\ y_{c4} \\ z_{c4} \end{pmatrix} \tag{5}$$

We have developed a numerical scheme for calculating $V_{R\text{-}nmp}$ between Body 1 and a sliced piece of Body 2 based on previous works.[30,31] To use the existing analytical relation between the two bodies, the sliced pieces of Body 2 were placed parallel to Body 1 with maintaining the rotation angles of Body 2. The detailed calculation procedures for van der Waals interactions are described in section 1 of SI. Then, vdW forces (F_{vdW}) and torques (τ_{vdW}) were calculated by a centered difference with displacement in length or angle as shown in section 2 of SI (Fig. S1 and Table S1).

2.2. Numerical construction of cubic particles and surface roughness

To study the effects of surface roughness on the vdW interaction, the rough surface was created by constructing asperities on the smooth cubes, as illustrated in Fig. 2a. First, a cube body was transformed translationally in order that its center position became (0,0,0). Then, the surface represented by a positive unit vector in the x-direction was classified into two sets of 50 points as $2\ T_1$ and $2L_1$ (the total number of the asperities is 2500) and constructed the roughness layer as $0.2\ W_1$. Next, the height of each divided point in the roughness layer was determined by adding a Gaussian random number into $0.2\ W_1$ at a given root-mean-square roughness (RMS). Using the inversion symmetry process (e.g., equating the roughness height of (x, y, z) to the roughness height of (-x, -y, -z) based on the (0,0,0) center of mass), the asperities of the surface represented by a negative unit vector in the x-direction for surface roughness were determined. The dimensions of constructed asperities were defined as $2L_1 = 0.04$, $2\ T_1 = 0.04$, and $2\ W_1 =$ the height of asperities determined by randomly generated Gaussian numbers. In the meantime, the asperities were constructed 2500 asperities of each surface represented by a positive/negative unit vector in the y-direction with $2\ W_1 = 0.04$, $2L_1 = 0.04$, and $2\ T_1 =$ the height of asperities for the surface and 2500 asperities of each surface represented by a positive/a negative unit vector in z-direction with $2\ T_1 = 0.04$, $2\ W_1 = 0.04$, and $2L_1 =$ the height of asperities. Subsequently, the asperities of coordination for the other cuboid surfaces were determined using the same method. This procedure conserves a total particle volume within a small error (typically about 0.08 %). After creating asperities on the cuboid's surface, all asperities as well as the unchanged layer of the body were rotated by the defined rotational angles (θ_x, θ_y and θ_z) and translated into the original center point. The vdW interaction was then calculated by numerical summation,

$$V_R = V_{unchangedlayer} + \sum\sum V_{asperities} \tag{6}$$

3. Results & discussion

3.1. Van der Waals torque between smooth cubes and effect of particle size

In the first set of simulations, we calculated the vdW interactions between smooth cubic particles of identical size (Fig. 3a). We considered a parallel face-face configuration with various particle separations and relative orientations. While the vdW force (F_{vdW}) was monotonically increasing as a function of particle separation (Fig S2),[30] several interesting features can be resolved in the vdW torque (τ_{vdW}). Specifically, τ_{vdW} was calculated as a function of the x-axis rotation angle (θ_x) at cube separations of $h/L_1 = 0.1$, $h/L_1 = 0.15$, and $h/L_1 = 0.3$, respectively. Body-1 with $L_1 = T_1 = W_1 = 1$ was fixed at (0, 0, 0), while Body-2 with $L_2 = T_2 = W_2 = 1$ was placed at (2.1, 0, 0), (2.15, 0, 0), and (2.3, 0, 0). As Body-2 was rotated about the x-axis, τ_{vdW} decreased sharply from

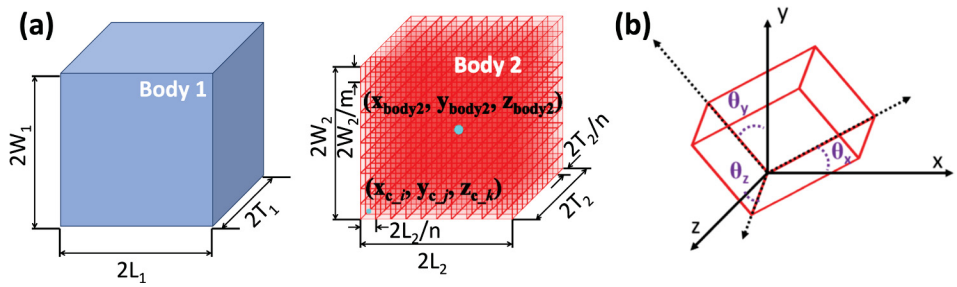

Fig. 1. Schematics showing (a) dimensions of a cube and sliced constituent small pieces in Body 2 for calculations of vdW interaction potentials., and (b) rotational angles θ_x, θ_y, and θ_z of a cube.

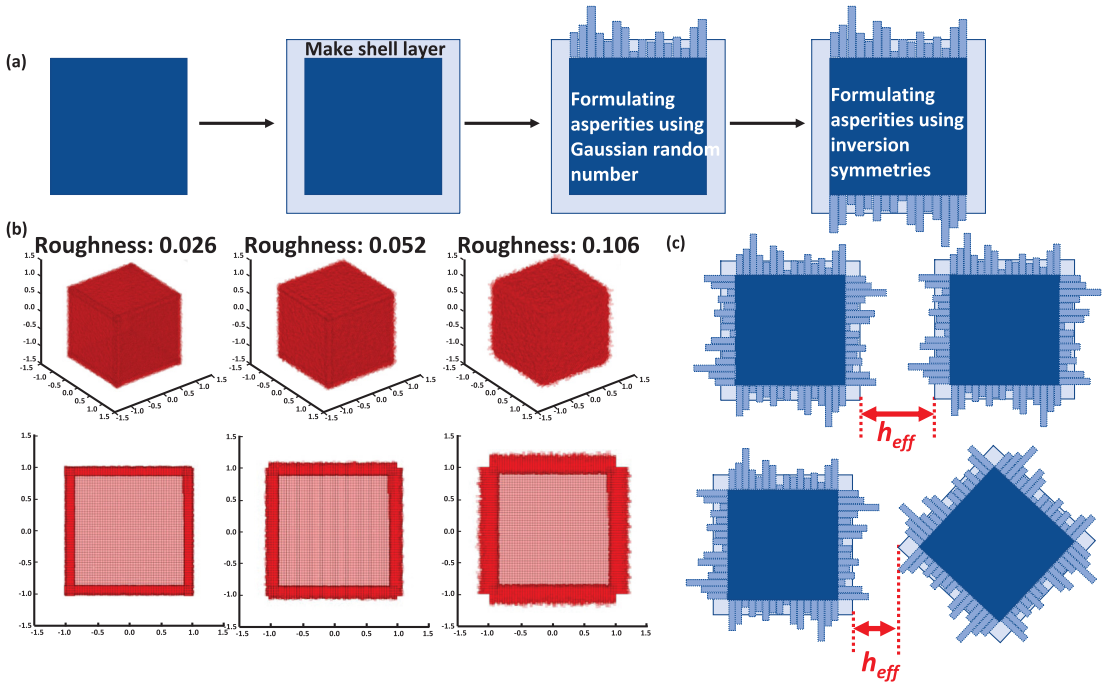

Fig. 2. Schematics showing (a) construction of asperities to produce surface roughness without displacing the center of mass, (b) constructed asperities on cubes with 0.026, 0.052, and 0.106 roots mean square (RMS) roughness and (c) definition of the effective separation distance between the cubes having randomly generated surface roughness.

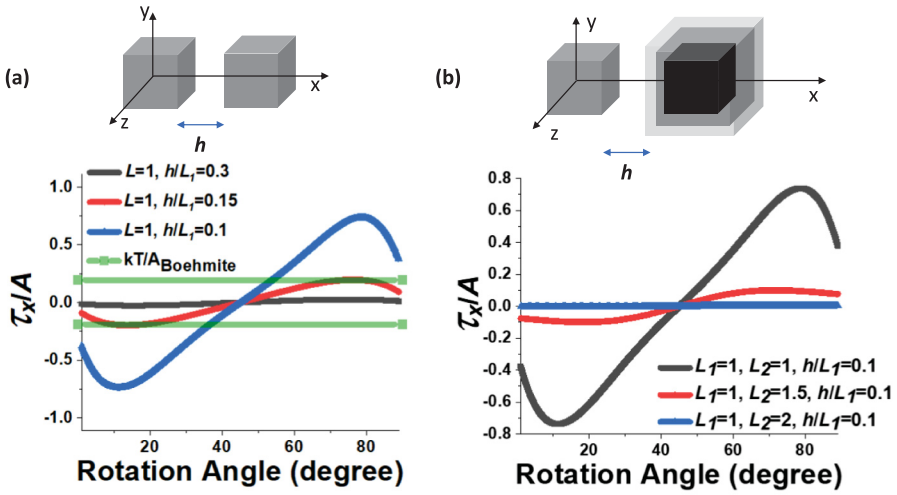

Fig. 3. Normalized van der Waals interaction torques (τ/A) as a function of rotation angle (θ_x) between cubes having smooth surfaces at (a) different normalized separation distance (h/L_1) and (b) different cube sizes of Body 2.

zero in the perfectly aligned configuration to a peak at approximately $\theta_x = 11^\circ$ and then decreased linearly back to zero as θ_x approached 45°. The symmetric case occurred in the second half-rotation; τ_{vdW} positively increased as θ_x approached 79° and returned to 0 as θ_x was increased to 90°, corresponding to another configuration with perfect cube alignment. A similar trend was observed at the various particle separations, with the overall magnitude of τ_{vdW} significantly increasing when h/L was decreased. For example, the maximum τ_{vdW} at $h/L = 0.1$ was 28.4 times larger than that at $h/L = 0.3$, with the peak relative angle shifting slightly from $\theta_x = 11^\circ$ to 18°.

Moreover, we investigated the effect of size disparity on the vdW interactions between the two particles ($L_2/L_1 = 1$, $L_2/L_1 = 1.5$, and $L_2/L_1 = 2$) on τ_{vdW} (Fig. 3b) and F_{vdW} (Fig. S3) was investigated at $h/L_1 = 0.1$. As shown in Fig. 3b, the 1:1.5 and 1:2 size ratio produced one and two orders of magnitude lower τ_{vdW}, respectively, compared to the equal-sized cubic pairs. As the L_2 size was increased to $L_2/L_1 = 1.5$, and $L_2/L_1 = 2$, the maximum τ_{vdW} was decreased to 9.97×10^{-2} (Ratio = 1/7.39) and 3.53×10^{-3} (Ratio = 1/208.83), respectively, compared to 7.37×10^{-1} at $L_2/L_1 = 1$, which follows exponential decrease. (See Fig. S4a) The configurations with $\tau_{vdW} = 0$ correspond to isotropic vdW interactions, indicating no torque that attempts to re-align the particles at distinct relative orientations. This result already presents a drastic departure from spherical particles that do not experience such torques. As the difference between Body 1 and Body 2 increased, the rotation of the Body 2 would become less sensitive to the Body 1, although the interaction potential (and the force) increases as the size difference increases. (Fig. S3a-c) The shape effect can be thus maximized at equal-size conditions. (Fig. S3 and S4) Similar phenomena were observed in

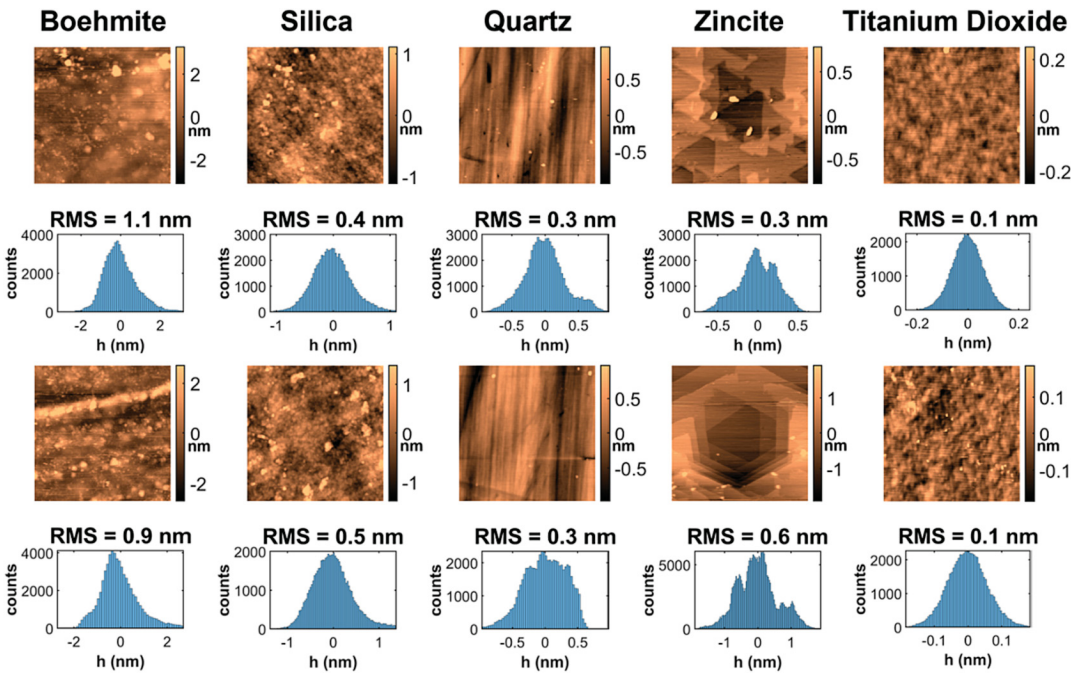

Fig. 4. Representative surface roughness of boehmite, silica, quartz, zincite, and titanium dioxide.

the face-to-edge configuration. (Fig. S5) To gain more physical insights on the scale of van der Waals interactions, we compared τ_{vdW} to the Brownian torque, which is associated with rotational diffusion in the order of kT. [26] Note that the balance between τ_{vdW} and τ_{Br} can be evaluated as kT/A for any given system because the τ_{vdW} scales by the Hamaker constant. As an example, we consider boehmite – an aluminum oxyhydroxide mineral that undergoes oriented nanocrystal attachment – with $A_{Boehmite} = 5.2\ kT$. [21] We determine that τ_{vdW} outcompetes the Brownian torque over the majority of relative orientations, spanning θ_x values of 1°–35° and 55°–89° when h/L is smaller than 0.15. By comparison, kT/A_{gold} is ~ 0.01645 based on the Hamaker constant for a gold-water-gold system (A_{gold} = 60.8 kT) [32], such that the metal particles could begin aligning towards the face-to-face arrangement at $h/L < 0.3$. This analysis demonstrates that anisotropic particle shapes could result in significant vdW torques that impact assembly pathways depending on system-specific properties. [8].

3.2. Effects of surface roughness-symmetric configurations

The second set of simulations explored the effect of surface roughness on vdW interactions. To inform the numerical parameters using experimental data, we performed atomic force microscopy (AFM) imaging of common minerals, including crystalline and amorphous materials, metal oxides and hydroxides, as well as surfaces covered with various heterogeneities and adsorbates. Fig. 4 shows example surfaces with roughness values between 0.3 and 1.1 nm, defined as the root mean square (RMS) of the surface topography. Note that the roughness of these samples is relatively small compared to natural minerals or nanoparticle systems, which is attributed to the etching treatments to create a smooth surface. Considering a reasonable range for nanoparticle size of 5–40 nm, the experimental values lead to rescaled RMS values ranging from 0.015 to 0.110. This range can be covered by utilizing 0.026, 0.052, and 0.105 as numerical RMS values for a normalized cube of size 2. Note that the 5–40 nm cubes having 0.5–1 nm RMS are indeed consistent with metal and mineral nanocrystals reported in many previous studies. For example, G. Zhu et al. reported that oriented attachment crystallizations could produce enigmatic textures with rough surfaces (±2.5 nm surface altitude difference of 100 nm particles) compared to ion-by-ion crystal growth which produces a relatively smooth surface (<1 nm surface altitude difference of 100 nm particles). [33] Using the rescaled RMS values, we studied the dependence of the vdW interactions (V_{vdW}) on the separation between two identical

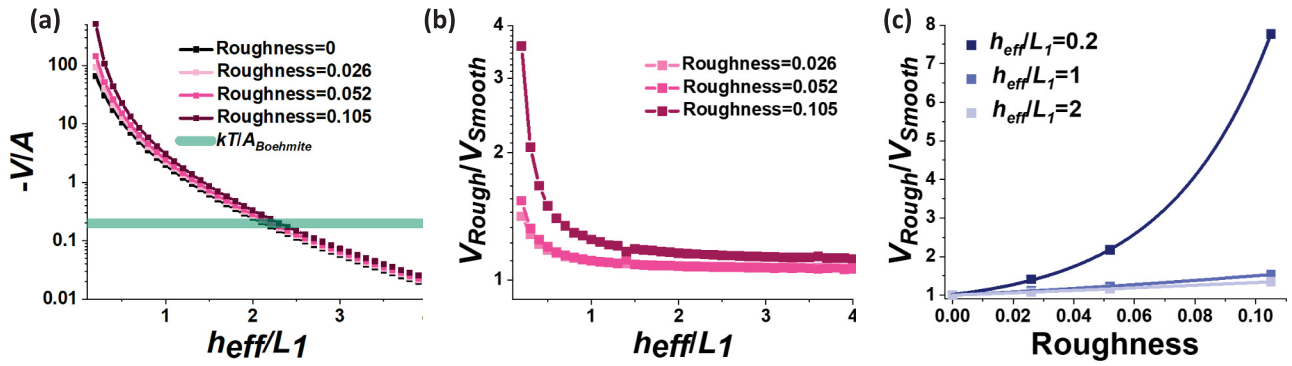

Fig. 5. (a) van der Waals interaction potential (V_{vdW}) as a function of the normalized effective separation (h_{eff}/L_1) between cubes having different surface roughness (Roughness = 0, 0.026, 0.052, and 0.105). (b) Comparison of $V_{Rougness}/V_{Smooth}$ as a function of h_{eff}/L_1 for different surface roughness. (c) $V_{Roughness}/V_{Smooth}$ as a function of surface roughness at h_{eff}/L_1 = 0.2,1 and 2.

particles with the selected values for surface roughness. The center of mass of Body 1 was set at $x = 0$, $y = 0$, and $z = 0$, and Body 2 was offset along the x-axis. The relative angles between Body 1 and Body 2 were $\theta_x = 0$, $\theta_y = 0$, and $\theta_z = 0$ to formulate face-to-face configurations. We observed that the increasing surface roughness increases V_{vdW} over the entire h/L range, as shown in Fig. 5. This result is attributed to the protrusions on rougher surfaces, which amplify the short-range behavior of the V_{vdW}. Our observation is consistent with the effect of roughness on the Casimir force calculated using the proximity force approximation. [34].

In the next set of simulations, we explored the configurations that do not induce a vdW torque because of symmetry in the relative orientations. (See Table S2 in the SI) This definition of h_{eff} presented here facilitates the systematic data interpretation for surface roughnesses defined Gaussian distributions. However, we reiterate that various types of surface roughness exist, and a clear definition of h_{eff} for more complex morphologies is not trivial. Fig. 6 shows F_{vdW} vs h_{eff}/L_1 between two identical particles at six representative configurations, namely face-to-face, face-to-edge, face-to-point, edge-to-edge, edge-to-point, and point-to-point. In all these configurations, the strength of the vdW interaction increased with increasing surface roughness. However, this effect was more noticeable for the face-to-face, face-to-edge and edge-to-edge configurations, particularly at $h_{eff}/L_1 \leq 1$. The 0.105 surface roughness produced 2.08-, 1.73-, and 2.72-time higher F_{vdW} than smooth cubes at 0.7, h_{eff}/L_1, respectively. This discrepancy increased to a full order of magnitude at $h_{eff}/L_1 = 0.7$ between rough cubes compared to smooth cubes. In contrast, the face-to-point, edge-to-point and point-to-point showed less drastic dependence on the surface roughness. For example, the cube with 0.105 surface roughness can generate 1.64, 1.81, and 1.56 times higher F_{vdW} than smooth cuboids at $h_{eff}/L_1 = 0.7$.

To put these results in perspective, we again examined the cases of boehmite and gold nanocrystals as model mineral and metal systems. The rough surface (RMS = 0.105) increased the crossover particle separation for which the vdW force dominates the Brownian force to ~ 0.17 L in boehmite and ~ 0.21 L in gold. (Fig. S6) These values correspond to separations of approximately 1–8 nm in particle sizes of 5–40 nm. Also, considering the Brownian torque on the cube that continuously changes the particle configurations, the results in Fig. 6 imply that the surface roughness can induce preferential mutual orientations, i.e., face-to-face, face-to-edge, and edge-to-edge, over the other configurations during particle aggregation. The effect of surface roughness on the torque is significant, but less drastic compared to the change in particle shape from smooth spheres to smooth cubes.

3.3. Effects of surface roughness-mismatched configurations

In addition to the configurations described above, we investigated mismatched configurations where one of the cubes was not placed along any of the primary coordinate axes (Fig. 7a). These simulations explored how τ_{vdW} can induce rotational motions from arbitrary starting positions to align the particles along specific orientations. Fig. 7 shows τ_{vdW} between identical cubes (length $2L$) with a mismatched face-to-face configuration. The center of mass of Body-1 was placed at (0,0,0), while the center of mass of Body-2 was placed at y = 0 and z = -0.45, with its x-coordinate varied to tune the particle separation h. All these configurations produced stronger torques with rougher surfaces. For metal nanoparticles (e.g., gold), rough surfaces can increase τ_{vdW} significantly to override the magnitude of the thermal motions at a large separation (i.e., $h_{eff}/L_1 > 1$). For minerals with smaller Hamaker constants (e.g., boehmite), τ_{vdW} becomes dominant at relatively shorter separations: $h_{eff}/L_1 < 1.25$ for face-to-face configurations and face-to-edge configurations and $h_{eff}/L_1 < 0.7$ for face-to-point configurations. These results indicated that rough surfaces promote rotational movement and specific alignment between particles, at least from an energetic point of view.

Moreover, we observed that rough surfaces can increase the vdW force when a particle undergoes translational motion in the vicinity of another particle (Fig. 8). To demonstrate this effect, Body 1 was set at

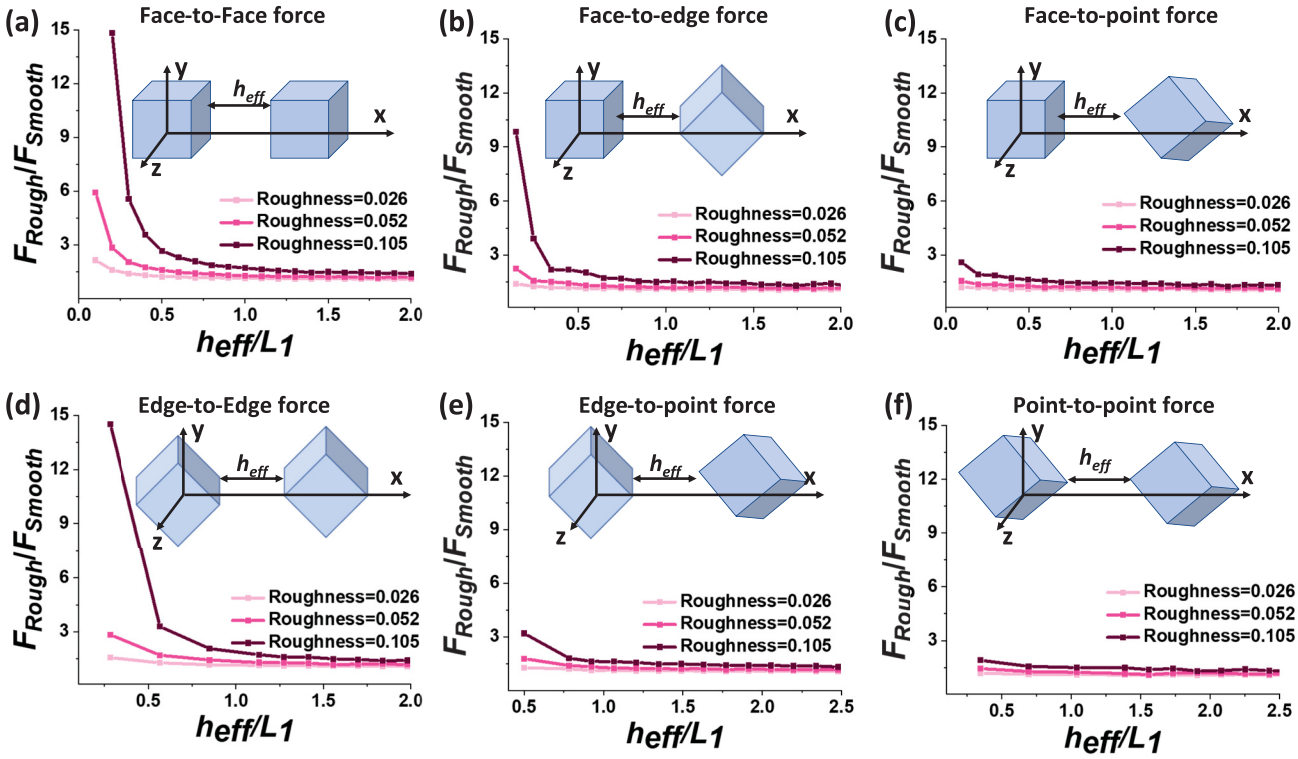

Fig. 6.V. an der waals interaction forces between rough surfaces (f_{Rough}) divided by van der Waals interaction forces between smooth surfaces (F_{Smooth}) as a function of the h_{eff}/L_1 for different configurations: (a) face-to-face, (b) face-to-edge, (c) face-to-point, (d) edge-to-edge, (e) edge-to-point, and (f) point-to-point. The detailed parameters of the configurations are described in Table S2.

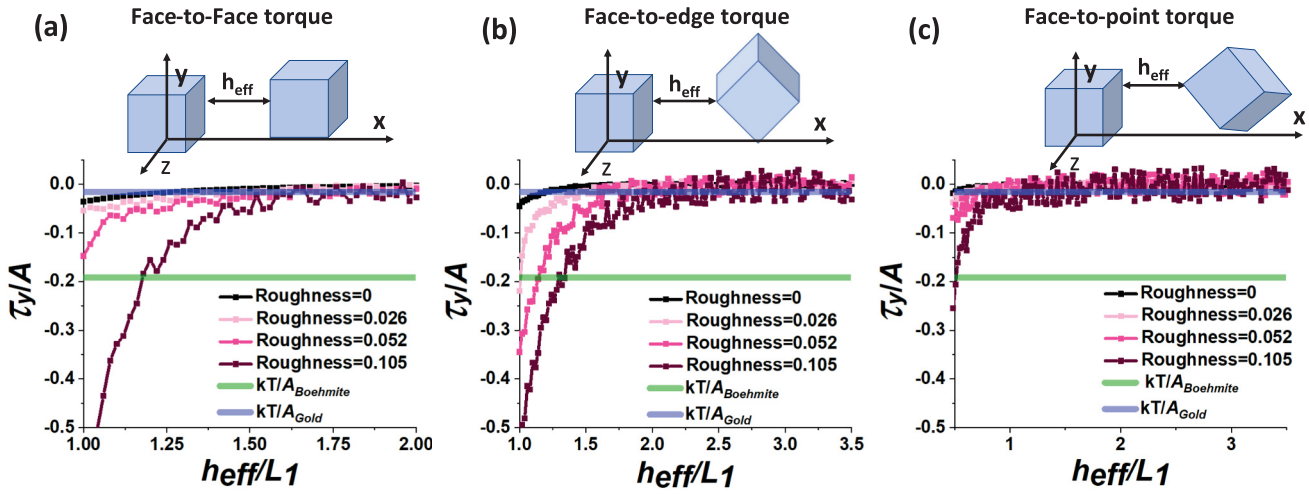

Fig. 7. Normalized van der Waals interaction torques (τ_y/A) as a function of h_{eff}/L_1 with various roughness conditions for (a) mismatched face-to-face configuration, (b) mismatched face-to-edge configuration, and (c) mismatched face-to-point configuration. To compare the thermal motion to rotational movements caused by van der Waals interaction torques in Boehmite and gold particles dispersed in water, kT/A of Boehmite and gold lines are plotted.

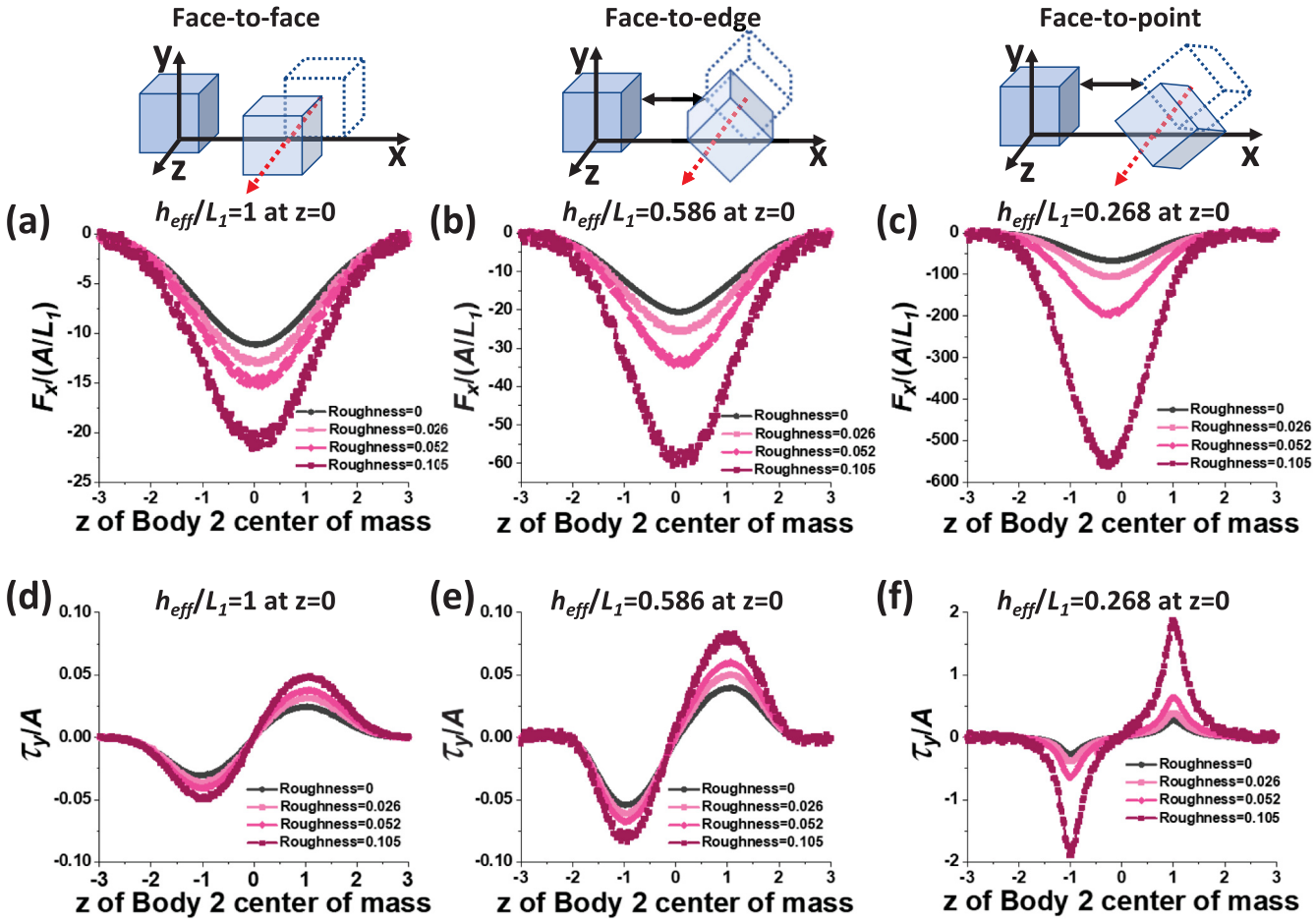

Fig. 8. (a-c) Normalized forces ($F_x/(A/L)$ and (d-f) normalized torques (τ_y/A) as a function of position z (with x = 3 and y = 0) of Body 2 center of mass with various surface roughness for different configurations: (a and d) face-to-face configuration, (b and e) face-to-edge configuration, and (c and f) face-to-point configuration.

(0,0,0) and another equal-sized Body 2 was moved from z = -3 to 3 with x and y fixed at 3 and 0, respectively. Again, three cases were sampled corresponding to face-to-face configurations, face-to-edge configurations and face-to-point configurations. In all cases, the magnitude of the x-component F_{vdW} peaked as Body 2 approached z = 0 and decreased again as the cube was displaced further. Concurrently, a strong negative τ_{vdW} maximized at z = -1, then decreased to zero as the anisotropic vdW interactions were nullified at z = 0. Similar to the earlier results, the surface roughness effect was ascribed to the protruded asperities decreasing the effective h between the surfaces, thus increasing F_{vdW} and

τ_{vdW}. Fig. 8b and c showed that F_{vdW} and τ_{vdW} of face-to-edge configurations and particularly face-to-point configurations were much stronger than those of face-to-face configurations at the same z of Body 2 center of mass. The underlying reason is that the rotation of Body 2 can reduce the effective separation distance. For example, the h/L decreased from 1 to 0.586 and 0.286, when the configuration was changed from face-to-face configuration to face-to-edge and face-to-point configuration respectively. This decreased h can generate much stronger F_{vdW} and τ_{vdW}, and thus the aggregation processes can be accelerated, as a rotating particle takes multiple configurations.

Not that at the randomness of rough surface construction, the deviated points were generated at the rough surface conditions in Fig. 6, Fig. 7 and Fig. 8 because of the random generation number based on the Gaussian distribution. The deviations were enhanced as the surface roughness and separation distance increased.

3.4. Effects of particle shape and surface roughness on particle dynamics and aggregation

To obtain further physical insights, we examined the scaling of V as a function of h_{eff}/L_1 for each surface roughness (Fig. 9). We considered two distinct regimes (Fig. 6d, Table 1). Firstly, for small particle separations of $h_{eff}/L_1 < 0.5$, the exponents of the power-law fits were −2.28, −2.40, −2.54, and −2.98 for RMS = 0, 0.026, 0.051, 0.105, respectively. Here, the exponent for the smooth case is comparable to the one from the known analytical formulation (i.e., 2),[6] providing further support for the validity of our analysis. Our results showed that the surface roughness changes the separation dependence of the interaction from $O(h^{-2})$ to $O(h^{-3})$, becoming stronger at closer separations. In the second regime of larger particle separations of $h_{eff}/L_1 > 0.5$, the power-law fits converge to an exponent of approximately −4, independent of surface roughness. This result indicates a cutoff length for the effect of nanoparticle surface roughness; the second scaling is a consequence of the Derjaguin approximation that is known to become inaccurate at separations comparable to the particle size.

In principle, the particle shape and surface roughness at microscopic and particle scales can also influence emergent phenomena due to inherent scale coupling that has been recognized in particle aggregation and attachment. To understand the effect of particle shape and surface roughness on particle dynamics and aggregation, while connecting to an interaction force, one needs to consider a generalized mobility relation for relative motion between two particles, $u = MF$, assuming that particle inertia is negligible: a reasonable assumption for nanoparticles in general. Here, u is the relative velocity, M is the hydrodynamic mobility, and F is a relevant force between two particles, in this case, F_{vdW}. We

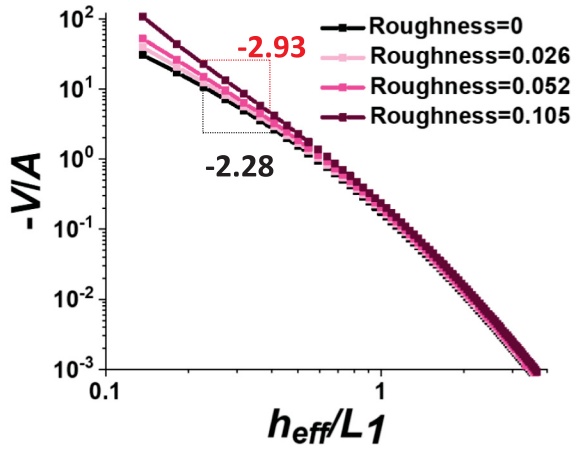

Fig. 9. Scaling of the normalized van der Waals interaction potential (-V/A) as a function of the normalized separation distance (h_{eff}/L_1) at a face-to-face configuration for various surface roughness.

Table 1
The linear fitting parameters of log scaled -V/A vs log scaled h_{eff}/L_1 according to surface roughness.

Roughness	$h_{eff}/L_1 = 0 \sim 0.5$		$h_{eff}/L_1 = 1 \sim 2$	
	Slope	Intercept	Slope	Intercept
0	−2.93	−1.52	−3.98	−1.60
0.026	−2.54	−1.46	−3.95	−1.66
0.052	−2.40	−1.45	−3.93	−1.69
0.105	−2.28	−1.45	−3.91	−1.73

applied a scaling analysis at a close separation of $\varepsilon \ll O(1)$ along the line of two centers of mass, where ε is a normalized separation scaled by the radius of a spherical particle or a half-length of a cubic particle. Furthermore, we considered a face-face configuration in the case of cubic particles for simplicity to establish a direct comparison with the case of spherical particles.

For spherical particles, $M \sim O(\varepsilon)$ and $F_{vdW} \sim O(1/\varepsilon^2)$,[6] leading to $u \sim O(1/\varepsilon)$, indicating that the approaching velocity between two spherical particles becomes larger as the separation decreases. However, for smooth cubic particles, Xiao et al.'s work showed that $M \sim O(\varepsilon^3)$ in the face-face configuration from the hydrodynamic interaction calculations by a boundary element method, utilizing an integral representation of the Stokes flow via a hydrodynamic Green's function (i.e., the Oseen tensor).[35] Since $F_{vdW} \sim O(1/\varepsilon^3)$ as shown in the current work, we obtain $u \sim O(1)$. That is, the approaching velocity becomes independent of separation at $h_{eff}/L_1 \ll 1$. Because the motion driven by F_{vdW}, a key attractive force, would be directly responsible for collision events leading to particle aggregation and attachment, this result illustrates a qualitative difference between cubic and spherical particles. More importantly, a previous study based on the hydrodynamic theory would imply that the surface roughness of a particle would lead to $M \sim O(1)$, [36] leading to $u \sim O(1/\varepsilon^4)$ considering our result that $F_{vdW} \sim O(1/\varepsilon^4)$ for rough cubic particles. Such a large change in the velocity scaling for cubic particles suggests that the surface roughness of the cubic particle can induce a noticeable difference in kinetics of aggregation and attachment, even compared with the case for spherical particles.

Note that upon particle contact, it is plausible that the dispersion forces are in fact reduced for rough surfaces with a reduced contact area compared to smooth surfaces with full contact. [24,37] However, in that regime of very small particle separations, additional considerations come into play, such as interfacial solution structure, that are not captured by this model, and hence difficult to interpret. Furthermore, at close particle separations, additional dynamics and energetics come into play that can alter the aggregation outcomes including the enhancement of dispersion forces due to interfacial solutions structuring, [38] the effect of crystallographic symmetries on the energy landscape, [39,40] and the forces associated with the expulsion of ions from the confined fluid. [41] It is thus highly plausible that particle aggregation is arbitrary and followed by sliding and rotation, or in fact ending in a metastable configuration.

4. Conclusions

Our results demonstrated the importance of particle shape and roughness on aggregation and assembly outcomes. By considering cubic particles, we calculated anisotropic vdW forces and torques that are inaccessible by spherical approximations. The magnitudes of these interactions were significant, often exceeding the Brownian motion of nanoparticles. Interestingly, incorporating roughness in the cube surfaces further increased the van der Waals interactions compared to smooth surfaces. This result was consistent in all the sampled geometries and parameters, but its significance depended on the specifics of particle chemistry, size disparity, and the extent of surface roughness.

Our results are particularly important in the context of the driving forces for oriented particle attachment, wherein two approaching

particles align their crystallographic axes prior to a collision and attachment event. Recent studies showed that van der Waals forces between two interacting nanocrystals can have an anisotropic nature that mirrors the crystallographic symmetries of the particles involved. [42–44] Other studies showed that the distribution of ions and water molecules at the interface is templated by the crystallographic symmetries of the particles, which assists in aligning them prior to the collision. [41,45,46] While these mechanistic features are clearly relevant to the attachment process, the current study presents an important key result: anisotropic particles are conducive to oriented attachment purely for geometric reasons, even without considering any atomistic or crystallographic effects. Indeed, the significant torques between misaligned cubic particles can be sufficient to guide an oriented attachment process.

Another key result pertains to the coupling of dynamics and energetics in nanocrystal systems. Typically, an analysis of colloidal stability is performed by calculating interaction potentials for a given nanomaterial system, with limited consideration to dynamics effects. Furthermore, such formulations are often limited by approximations of spherical particles with smooth surfaces. Our data showed a drastic dependence of the scaling – beyond simply the magnitude – of vdW interactions on particle shape and roughness. By coupling to hydrodynamics, this effect is compounded and can thus be the arbiter of preventing or promoting particle aggregation. Future work should aim to apply the numerical schemes developed here to delineate the emergent behavior of whole particle ensembles, beyond pair-wise interactions.

Declaration of Competing Interest

The authors declare that they have no known competing financial interests or personal relationships that could have appeared to influence the work reported in this paper.

Data availability

Data and tools supporting the findings of this study are available from the corresponding authors on request

Acknowledgements

This work was supported by the Division of Chemical, Bioengineering, Environmental, and Transport Systems, National Science Foundation, under grant CBET-2132355. Development of the model, experiments, and detailed analyses were also supported by the Interfacial Dynamics in Radioactive Environments and Materials (IDREAM), an Energy Frontier Research Center funded by the U.S. Department of Energy (DOE), Office of Science, Basic Energy Sciences (FWP 68932). A preliminary development of the formulation and calculation schemes for the van der Waals forces/torques was supported by the US DOE, Office of Basic Energy Sciences, Division of Materials Science and Engineering, Synthesis and Processing Science Program at Pacific Northwest National Laboratory (PNNL), FWP 67554. PNNL is a multiprogram national laboratory operated for DOE by Battelle Memorial Institute under Contract No. DE-AC05-76RL0-1830.

Author Contributions

J.L and E.N contributed equally to this work. J.L designed the studies, developed the models and conducted theoretical calculations. E. N assisted the development of the models, conducted data discussion, and supervised AFM experiments. J.H conducted AFM experiments. D.L conducted AFM data analysis. B.L conducted discussions on the study design and model development. G.S supervised the development of the models. C.P conducted the discussions for model developments. H.M conducted the discussions for model development. J.C designed and supervised the work, assisted the model development, and conducted data discussions/analyses.

Appendix A. Supplementary data

Supplementary data to this article can be found online at https://doi.org/10.1016/j.jcis.2023.08.160.

References

[1] J. Lee, E. Nakouzi, M. Song, B. Wang, J. Chun, D. Li, Mechanistic Understanding of the Growth Kinetics and Dynamics of Nanoparticle Superlattices by Coupling Interparticle Forces from Real-Time Measurements, ACS Nano 12 (12) (2018) 12778–12787.
[2] J. Lee, E. Nakouzi, D. Xiao, Z. Wu, M. Song, C. Ophus, J. Chun, D. Li, Interplay between Short-and Long-Ranged Forces Leading to the Formation of Ag Nanoparticle Superlattice, Small 1901966 (2019).
[3] D. Li, Q. Chen, J. Chun, K. Fichthorn, J. De Yoreo, H. Zheng, Nanoparticle Assembly and Oriented Attachment: Correlating Controlling Factors to the Resulting Structures, Chem. Rev. (2023).
[4] J.J. De Yoreo, E. Nakouzi, B. Jin, J. Chun, C.J. Mundy, Spiers Memorial Lecture: Assembly-based pathways of crystallization, Faraday Discuss. (2022).
[5] R.A. Peterson, E.C. Buck, J. Chun, R.C. Daniel, D.L. Herting, E.S. Ilton, G. J. Lumetta, S.B. Clark, Review of the scientific understanding of radioactive waste at the US DOE Hanford Site, Environ. Sci. Tech. 52 (2) (2018) 381–396.
[6] W.B. Russel, W. Russel, D.A. Saville, W.R. Schowalter, Colloidal dispersions, Cambridge university press1991.
[7] W. Russel, D. Saville, W. Schowalter, Colloidal Dispersions Cambridge Univ, Press Cambridge, 1989.
[8] U. Anand, J. Lu, D. Loh, Z. Aabdin, U. Mirsaidov, Hydration layer-mediated pairwise interaction of nanoparticles, Nano Lett. 16 (1) (2016) 786–790.
[9] A.S. Powers, H.-G. Liao, S.N. Raja, N.D. Bronstein, A.P. Alivisatos, H. Zheng, Tracking nanoparticle diffusion and interaction during self-assembly in a liquid cell, Nano Lett. 17 (1) (2017) 15–20.
[10] H. Hu, F. Ji, Y. Xu, J. Yu, Q. Liu, L. Chen, Q. Chen, P. Wen, Y. Lifshitz, Y. Wang, Reversible and precise self-assembly of Janus metal-organosilica nanoparticles through a linker-free approach, ACS Nano 10 (8) (2016) 7323–7330.
[11] H. Cölfen, M. Antonietti, Mesocrystals: inorganic superstructures made by highly parallel crystallization and controlled alignment, Angew. Chem. Int. Ed. 44 (35) (2005) 5576–5591.
[12] Q. Chen, H. Cho, K. Manthiram, M. Yoshida, X. Ye, A.P. Alivisatos, Interaction potentials of anisotropic nanocrystals from the trajectory sampling of particle motion using in situ liquid phase transmission electron microscopy, ACS Cent. Sci. 1 (1) (2015) 33–39.
[13] L. Liu, E. Nakouzi, M.L. Sushko, G.K. Schenter, C.J. Mundy, J. Chun, J.J. De Yoreo, Connecting energetics to dynamics in particle growth by oriented attachment using real-time observations, Nat. Commun. 11 (1) (2020) 1–11.
[14] S. Pednekar, J. Chun, J.F. Morris, Simulation of shear thickening in attractive colloidal suspensions, Soft Matter 13 (9) (2017) 1773–1779.
[15] A. Singh, S. Pednekar, J. Chun, M.M. Denn, J.F. Morris, From yielding to shear jamming in a cohesive frictional suspension, Phys. Rev. Lett. 122 (9) (2019), 098004.
[16] S. Pednekar, J. Chun, J.F. Morris, Bidisperse and polydisperse suspension rheology at large solid fraction, J. Rheol. 62 (2) (2018) 513–526.
[17] V.A. Parsegian, Van der Waals forces: a handbook for biologists, chemists, engineers, and physicists, Cambridge University Press, 2005.
[18] P.J. Scales, S.B. Johnson, T.W. Healy, P.C. Kapur, Shear yield stress of partially flocculated colloidal suspensions, AIChE J 44 (3) (1998) 538–544.
[19] Z. Zhou, P.J. Scales, D.V. Boger, Chemical and physical control of the rheology of concentrated metal oxide suspensions, Chem. Eng. Sci. 56 (9) (2001) 2901–2920.
[20] J. Chun, T. Oh, M. Luna, M. Schweiger, Effect of particle size distribution on slurry rheology: Nuclear waste simulant slurries, Colloids Surf A Physicochem Eng Asp 384 (1–3) (2011) 304–310.
[21] E. Nakouzi, J.A. Soltis, B.A. Legg, G.K. Schenter, X. Zhang, T.R. Graham, K. M. Rosso, L.M. Anovitz, J.J. De Yoreo, J. Chun, Impact of solution chemistry and particle anisotropy on the collective dynamics of oriented aggregation, ACS Nano 12 (10) (2018) 10114–10122.
[22] A.J. Krzysko, E. Nakouzi, X. Zhang, T.R. Graham, K.M. Rosso, G.K. Schenter, J. Ilavsky, I. Kuzmenko, M.G. Frith, C.F. Ivory, Correlating inter-particle forces and particle shape to shear-induced aggregation/fragmentation and rheology for dilute anisotropic particle suspensions: A complementary study via capillary rheometry and in-situ small and ultra-small angle X-ray scattering, J. Colloid Interface Sci. 576 (2020) 47–58.
[23] F.W. DelRio, M.P. de Boer, J.A. Knapp, E. David Reedy Jr, P.J. Clews, M.L. Dunn, The role of van der Waals forces in adhesion of micromachined surfaces, Nature materials 4(8) (2005) 629-634.
[24] D.F. Parsons, R.B. Walsh, V.S. Craig, Surface forces: Surface roughness in theory and experiment, J. Chem. Phys. 140 (16) (2014), 164701.
[25] V. Parsegian, G.H. Weiss, Dielectric anisotropy and the van der Waals interaction between bulk media, J. Adhes. 3 (4) (1972) 259–267.
[26] J. Chun, J.-L. Li, R. Car, I.A. Aksay, D.A. Saville, Anisotropic adsorption of molecular assemblies on crystalline surfaces, J. Phys. Chem. B 110 (33) (2006) 16624–16632.
[27] D. Saville, J. Chun, J.-L. Li, H. Schniepp, R. Car, I.A. Aksay, Orientational order of molecular assemblies on inorganic crystals, Phys. Rev. Lett. 96 (1) (2006), 018301.
[28] H.C. Hamaker, The London—van der Waals attraction between spherical particles, Physica 4 (10) (1937) 1058–1072.

[29] G. Nolze, Euler angles and crystal symmetry, Cryst. Res. Technol. 50 (2) (2015) 188–201.
[30] H. Maeda, Y. Maeda, Orientation-Dependent London–van der Waals Interaction Energy between Macroscopic Bodies, Langmuir 31 (26) (2015) 7251–7263.
[31] B.H.-j. Lee, G. Arya, Analytical van der Waals interaction potential for faceted nanoparticles, Nanoscale Horizons 5(12) (2020) 1628-1642.
[32] P. Pinchuk, K. Jiang, Size-dependent Hamaker constants for silver and gold nanoparticles, SPIE, Physical Chemistry of Interfaces and Nanomaterials XIV, 2015, pp. 168–174.
[33] G. Zhu, M.L. Sushko, J.S. Loring, B.A. Legg, M. Song, J.A. Soltis, X. Huang, K. M. Rosso, J.J. De Yoreo, Self-similar mesocrystals form via interface-driven nucleation and assembly, Nature 590 (7846) (2021) 416–422.
[34] P. Van Zwol, G. Palasantzas, J.T.M. De Hosson, Influence of random roughness on the Casimir force at small separations, Phys. Rev. B 77 (7) (2008), 075412.
[35] D. Xiao, Z. Wu, M. Song, J. Chun, G.K. Schenter, D. Li, Silver nanocube and nanobar growth via anisotropic monomer addition and particle attachment processes, Langmuir 34 (4) (2018) 1466–1472.
[36] J.T. Jenkins, M. Koenders, Hydrodynamic interaction of rough spheres, Granul. Matter 7 (2005) 13–18.
[37] B.H.-j. Lee, G. Arya, Assembly mechanism of surface-functionalized nanocubes, Nanoscale 14(10) (2022) 3917-3928.
[38] J. Chun, C.J. Mundy, G.K. Schenter, The role of solvent heterogeneity in determining the dispersion interaction between nanoassemblies, J. Phys. Chem. B 119 (18) (2015) 5873–5881.
[39] B.A. Legg, J.J. De Yoreo, Effects of Size and Shape on the Tolerances for Misalignment and Probabilities for Successful Oriented Attachment of Nanoparticles, Langmuir 39 (8) (2023) 2985–2994.
[40] M.V. Morrell, X. He, G. Luo, A.S. Thind, T.A. White, J.A. Hachtel, A.Y. Borisevich, J.-C. Idrobo, R. Mishra, Y. Xing, Significantly Enhanced Emission Stability of CsPbBr 3 Nanocrystals via Chemically Induced Fusion Growth for Optoelectronic Devices, ACS Applied Nano Materials 1 (11) (2018) 6091–6098.
[41] E. Nakouzi, S. Kerisit, B.A. Legg, S. Yadav, D. Li, A. Stack, C.J. Mundy, J. Chun, G. K. Schenter, J.J. De Yoreo, Solution Structure and Hydration Forces between Mica and Hydrophilic Versus Hydrophobic Surfaces, J. Phys. Chem. C 127 (5) (2023) 2741–2752.
[42] D. Li, J. Chun, D. Xiao, W. Zhou, H. Cai, L. Zhang, K.M. Rosso, C.J. Mundy, G.K. Schenter, J.J. De Yoreo, Trends in mica–mica adhesion reflect the influence of molecular details on long-range dispersion forces underlying aggregation and coalignment, Proceedings of the National Academy of Sciences 114(29) (2017) 7537-7542.
[43] X. Zhang, Y. He, M.L. Sushko, J. Liu, L. Luo, J.J. De Yoreo, S.X. Mao, C. Wang, K. M. Rosso, Direction-specific van der Waals attraction between rutile TiO2 nanocrystals, Science 356 (6336) (2017) 434–437.
[44] X. Zhang, Z. Shen, J. Liu, S. Kerisit, M. Bowden, M. Sushko, J. De Yoreo, K. M. Rosso, Direction-specific interaction forces underlying zinc oxide crystal growth by oriented attachment, Nat. Commun. 8 (1) (2017) 835.
[45] M. Raju, A.C. Van Duin, K.A. Fichthorn, Mechanisms of oriented attachment of TiO2 nanocrystals in vacuum and humid environments: reactive molecular dynamics, Nano Lett. 14 (4) (2014) 1836–1842.
[46] E. Nakouzi, A.G. Stack, S. Kerisit, B.A. Legg, C.J. Mundy, G.K. Schenter, J. Chun, J. J. De Yoreo, Moving beyond the solvent-tip approximation to determine site-specific variations of interfacial water structure through 3D force microscopy, J. Phys. Chem. C 125 (2) (2020) 1282–1291.

Supporting Information (SI) for

Effects of particle shape and surface roughness on van der Waals interactions and coupling to dynamics in nanocrystals

Jaewon Lee[a]*, Elias Nakouzi[b], Jaeyoung Heo[b], Benjamin A. Legg[b], Gregory K. Schenter[b], Dongsheng Li[b], Chanwoo Park[a], Hongbin Ma[a], Jaehun Chun[b,c]*

[a] Department of Mechanical and Aerospace Engineering, University of Missouri, 416 South 6th Street, Columbia 65211, United States

[b] Physical and Computational Sciences Directorate, Pacific Northwest National Laboratory, Richland, Washington 99352, United States

[c] Levich Institute and Department of Chemical Engineering, CUNY City College of New York; New York, New York 10031, United States

* To whom correspondence should be addressed: j.lee@missouri.edu and Jaehun.Chun@pnnl.gov

1. Calculation of $V_{R\text{-}nmp}$ between a Body-1 and a sliced piece of a Body 2

According to the given geometrical parameters (i.e., dimensions of length, thickness, and width of Body 1: $2L_1$, $2T_1$, $2W_1$; dimensions of length, thickness, and width of a sliced piece of a Body 2: $2L_2/n$, $2T_2/m$, $2W_2/p$; x-, y-, and z-directional separation distance: hx, hy, and hz), the integrations were calculated numerically based on a rectangular coordinate system,[1]

$$V_{R-nmp} = \sum_{k=1}^{4}\sum_{j=1}^{4}\sum_{i=1}^{4}(-1)^{i+j+k}V_{xyz} \quad \textbf{Error! Bookmark not defined.}\text{Eq. (S1)}$$

where V_{xyz} is

$$\begin{aligned} V_{xyz}(c_k, b_j, a_i) = \Bigg[& \left(\frac{c_k\left(a_i^2+b_j^2\right)^{3/2}}{24a_i^2b_j^2}\right)\tan^{-1}\left(\frac{c_k}{\sqrt{a_i^2+b_j^2}}\right) \\ & + \left(\frac{3}{32}\right)\left(\frac{c_k}{b_j}-\frac{b_j}{c_k}\right)\tan^{-1}\left(\frac{b_j}{c_k}\right) \\ & + \left(\frac{1}{24}\right)b_j\left(\frac{1}{a_i^2}+\frac{1}{c_k^2}\right)\sqrt{a_i^2+c_k^2}\,\tan^{-1}\left(\frac{b_j}{\sqrt{a_i^2+c_k^2}}\right) \\ & + \left(\frac{1}{24}\right)a_i\left(\frac{1}{b_j^2}+\frac{1}{c_k^2}\right)\sqrt{b_j^2+c_k^2}\,\tan^{-1}\left(\frac{a_i}{\sqrt{b_j^2+c_k^2}}\right) \\ & + \left(\frac{1}{32}\right)\ln\left(\frac{\left(b_j^2+c_k^2\right)^3}{c_k^2\left(a_i^2+b_j^2+c_k^2\right)^2}\right)\Bigg] \end{aligned} \quad \textbf{Error! Bookmark not defined.}\text{Eq. (S2)}$$

Here, a_i, b_j and c_k of Eq. S2 were determined according to the specific geometrical configurations, which were categorized into parallel-orienting configurations (Fig. S1a), coplanar configurations (Fig. S1b), and twisted configurations (Fig. S1c). The configurations were defined by the center position of the Body 1 (0,0,0) and a sliced piece of the Body 2 ($x_{c\text{-}e1}$, $y_{c\text{-}e2}$, $z_{c\text{-}e3}$), and relative angles (θ_x, θ_y, θ_z).

1) Parallel-orienting configurations: $\theta_x=\theta_y=\theta_z=0$ and $x_{c\text{-}e1}\neq y_{c\text{-}e2}\neq z_{c\text{-}e3}\neq 0$,

$$a_1 = hz + 2L_1; a_2 = hz + 2(L_1 + L_2/n); a_3 = hz + 2L_2/n; a_4 = hz;$$
$$b_1 = hy + 2W_1; b_2 = hy + 2(W_1 + W_2/p); b_3 = hy + 2W_2/p; b_4 = hy;$$
$$c_1 = hx + 2T_1; c_2 = hx + 2(T_1 + T_2/m); c_3 = hx + 2T_2/m; c_4 = hx; \quad \text{(S3)}$$

Error! Bookmark not defined.

2) Coplanar configuration: $\theta_x=\theta_z=0$, $\theta_y\neq 0$, $x_{c\text{-}e1}\neq z_{c\text{-}e3}\neq 0$ and $y_{c\text{-}e2}=0$

$$a_1 = hz + 2L_1; a_2 = hz + 2L_1 + pl; a_3 = hz + pl; a_4 = hz;$$
$$b_1 = hy + 2W_1; b_2 = hy + 2(W_1 + W_2/p); b_3 = hy + 2W_2/p; b_4 = hy;$$
$$c_1 = hx + 2T_1; c_2 = hx + 2T_1 + dhx; c_3 = hx + dhx; c_4 = hx; \quad \text{(S4)}$$

Error! Bookmark not defined.

3) Twisted configuration: $\theta_y=\theta_z=0$, $\theta_x\neq 0$, $x_{c\text{-}e1}\neq y_{c\text{-}e2}\neq z_{c\text{-}e3}\neq 0$

$$a_1 = hz + 2L_1; a_2 = hz + 2L_1 + pl; a_3 = hz + pl; a_4 = hz;$$
$$b_1 = hy + 2T_1; b_2 = hy + 2T_1 + dhy; b_3 = hy + dhy; b_4 = hy;$$
$$c_1 = hx + 2W_1; c_2 = hx + 2(W_1 + W_2/p); c_3 = hx + 2W_2/p; c_4 = hx; \quad \text{(S5)}$$

Error! Bookmark not defined.

Table S1. Parameters for calculating $V_{R\text{-}nmp}$ according to the configuration.

	Right Delta	Tetragon	Left Delta
Domain Height	$hdr = 2(L_2/n)\sin\theta$	$ht = (T_2/m)\cos\theta - (L_2/n)\sin\theta$	$hdl = 2(L_2/n)\sin\theta$
	$hdr = 2(T_2/m)\cos\theta$	$ht = (L_2/n)\sin\theta - (T_2/m)\cos\theta$	$hdl = 2(T_2/m)\cos\theta$
Δhx, Δhy	*hdr/s*	*ht/s*	*hdl/s*

pl	$\frac{2L_2/n}{\cos\theta} - q/\sin\theta\cos\theta$ $\frac{2T_2/m}{\sin\theta} - q/\sin\theta\cos\theta$	$\frac{2L_2/n}{\cos\theta}$ $\frac{2T_2/m}{\sin\theta}$	$q/\sin\theta\cos\theta$
zl	$z_{c-e3} - \frac{T_2/m}{\sin\theta} + (q + ht)/\tan\theta$	$z_{c-e3} - \frac{L_2/n}{\cos\theta} - (q - ht)\tan\theta$ $z_{c-e3} - \frac{T_2/m}{\sin\theta} + (q - ht)/\tan\theta$	$z_{c-e3} - \frac{L_2/n}{\cos\theta} - (q - ht - hdl)\tan\theta$
Configuration 2			
hx	$x_{c-e1} - T_1 + ht + q$	$x_{c-e1} - T_1 - ht + q$	$x_{c-e1} - T_1 - ht - hdl + q$
hy	$-2W_1$	$-2W_1$	$-2W_1$
hz	$zl - L_1$	$zl - L_1$	$zl - L_1$
Configuration 3			
hx	$x_{c-e1} - (w_1 + w_2/p)$	$x_{c-e1} - (w_1 + w_2/p)$	$x_{c-e1} - (w_1 + w_2/p)$
hy	$y_{c-e2} - T_1 + ht + q$	$y_{c-e2} - T_1 - ht + q$	$y_{c-e2} - T_1 - ht - hdl + q$
hz	$zl - L_1$	$zl - L_1$	$zl - L_1$

Additionally, other various configurations, which were defined as $\theta_y \neq \theta_z \neq \theta_x \neq 0$, $x_{c\text{-}e1} \neq y_{c\text{-}e2} \neq z_{c\text{-}e3} \neq 0$, would be estimated by the vector summaption of the a sliced piece of a Body 2 using the twisted configurations.

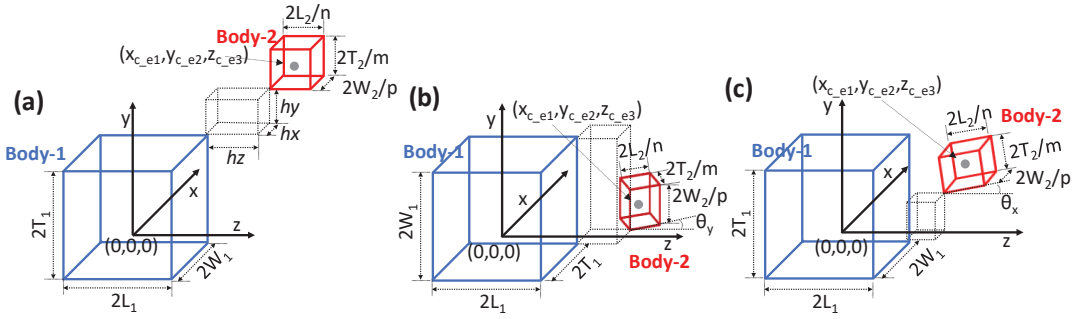

Fig. S1 Schematic drawing of (a) parallel-orienting rectangular Body -1 and a sliced piece of a Body-2, (b) Rectangular Body-1 and a sliced piece of a Body-2 in a coplanar configuration with θ_y, and (c) Rectangular Body-1 and a sliced piece of a Body-2 in a twisted configuration with θ_x.

2. Numerical differentiation.

A centered difference was applied to obtain vdW forces (F_{vdW}) and torques (τ_{vdW}) in each direction:

$$F_{vdW-x} = -\frac{\partial V_{vdW}}{\partial x} = -\frac{V_{vdW}(hx + \Delta d, hy, hz) - V_{vdW}(hx - \Delta d, hy, hz)}{2\Delta d} \quad \text{Error! Bookmark not defined.Eq. (S6)}$$

$$F_{vdW-y} = -\frac{\partial V_{vdW}}{\partial y} = -\frac{V_{vdW}(hx, hy + \Delta d, hz) - V_{vdW}(hx, hy - \Delta d, hz)}{2\Delta d} \quad \text{Eq. (S7)}$$

$$F_{vdW-z} = -\frac{\partial V_{vdW}}{\partial z} = -\frac{V_{vdW}(hx, hy, hz + \Delta d) - V_{vdW}(hx, hy, hz - \Delta d)}{2\Delta d} \quad \text{Error! Bookmark not defined.Eq. (S8)}$$

$$\tau_{vdW-\theta_x} = -\frac{\partial V_{vdW}}{\partial \theta_x} = -\frac{V_{vdW}(\theta_x + \Delta\theta, \theta_y, \theta_z) - V_{vdW}(\theta_x - \Delta\theta, \theta_y, \theta_z)}{2\Delta\theta} \quad \text{Error! Bookmark not defined.Eq. (S9)}$$

$$\tau_{vdW-\theta_y} = -\frac{\partial V_{vdW}}{\partial \theta_y} = -\frac{V_{vdW}(\theta_x, \theta_y + \Delta\theta, \theta_z) - V_{vdW}(\theta_x, \theta_y - \Delta\theta, \theta_z)}{2\Delta\theta} \quad \text{Eq. (S10)}$$

$$\tau_{vdW-\theta_z} = -\frac{\partial V_{vdW}}{\partial \theta_z} = -\frac{V_{vdW}(\theta_x, \theta_y, \theta_z + \Delta\theta) - V_{vdW}(\theta_x, \theta_y, \theta_z - \Delta\theta)}{2\Delta\theta} \quad \text{Error! Bookmark not defined.Eq. (S11)}$$

Data and tools supporting the findings of this study are available from the corresponding authors on request.

3. Configurations.

The center positions (x,y,z) and rotational angles (θ_x,θ_y,θ_z) of Body 1 and Body 2 for Fig. 6, Fig. 7, and Fig. 8 are described in Table S2, Table S3, and Table S4, respectively.

Table S2. Configurations of Fig. 6

	Face-to-Face	Face-to-Edge	Face-to-Point	Edge-to-Edge	Edge-to-Point	Point-to-Point
Scheme	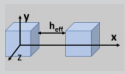	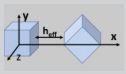	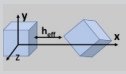	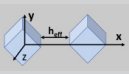	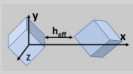	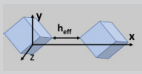
Center position of Body 1	X=0, y=0, z=0	X=0, y=0, z=0	X=0, y=0, z=0	X=0, y=0, z=0	X=0, y=0, z=0	X=0, y=0, z=0
Relative angle of Body 1	θ_x=0, θ_y=0, θ_z=0	θ_x=0, θ_y=0, θ_z=0	θ_x=0, θ_y=0, θ_z=0	θ_x=0, θ_y=0, θ_z=45	θ_x=0, θ_y=0, θ_z=45	θ_x=0, θ_y=45, θ_z=45
Center position of Body 2	X=from 0 to 4, y=0, z=0	X=from 0 to 4, y=0, z=0	X=from 0 to 4, y=0, z=0	X=from 0 to 4, y=0, z=0	X=from 0 to 4, y=0, z=0	X=from 0 to 4, y=0, z=0
Relative angle of Body 2	θ_x=0, θ_y=0, θ_z=0	θ_x=0, θ_y=0, θ_z=45	θ_x=0, θ_y=45, θ_z=45	θ_x=0, θ_y=0, θ_z=45	θ_x=0, θ_y=45, θ_z=45	θ_x=0, θ_y=45, θ_z=45

Table S3. Configurations of Fig. 7

	Face-to-Face	Face-to-Edge	Face-to-Point
Scheme	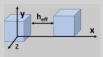		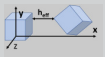
Center position of Body 1	X=0, y=0, z=0	X=0, y=0, z=0	X=0, y=0, z=0
Relative angle of Body 1	θ_x=0, θ_y=0, θ_z=0	θ_x=0, θ_y=0, θ_z=0	θ_x=0, θ_y=0, θ_z=0
Center position of Body 2	X=from 0 to 4, y=0, z=-0.45	X=from 0 to 4, y=0, z=-0.45	X=from 0 to 4, y=0, z=-0.45
Relative angle of Body 2	θ_x=0, θ_y=0, θ_z=0	θ_x=0, θ_y=0, θ_z=45	θ_x=0, θ_y=45, θ_z=45

Table S4. Configurations of Fig. 8

	Face-to-Face	Face-to-Edge	Face-to-Point
Scheme			
Center position of Body 1	X=0, y=0, z=0	X=0, y=0, z=0	X=0, y=0, z=0
Relative angle of Body 1	θ_x=0, θ_y=0, θ_z=0	θ_x=0, θ_y=0, θ_z=0	θ_x=0, θ_y=0, θ_z=0
Center position of Body 2	X=3, y=0, z=from -3 to 3	X=3, y=0, z=from -3 to 3	X=3, y=0, z=from -3 to 3
Relative angle of Body 2	θ_x=0, θ_y=0, θ_z=0	θ_x=0, θ_y=0, θ_z=45	θ_x=0, θ_y=45, θ_z=45

4. Additional results.

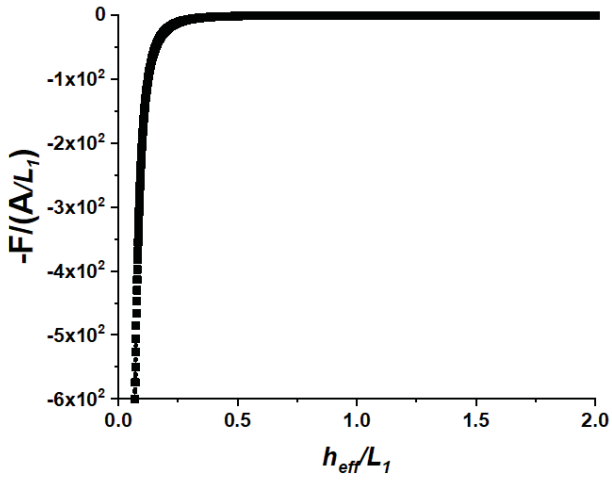

Fig. S1. F_{vdW} of cube-cube with face-to-face configurations as a function of separation distance.

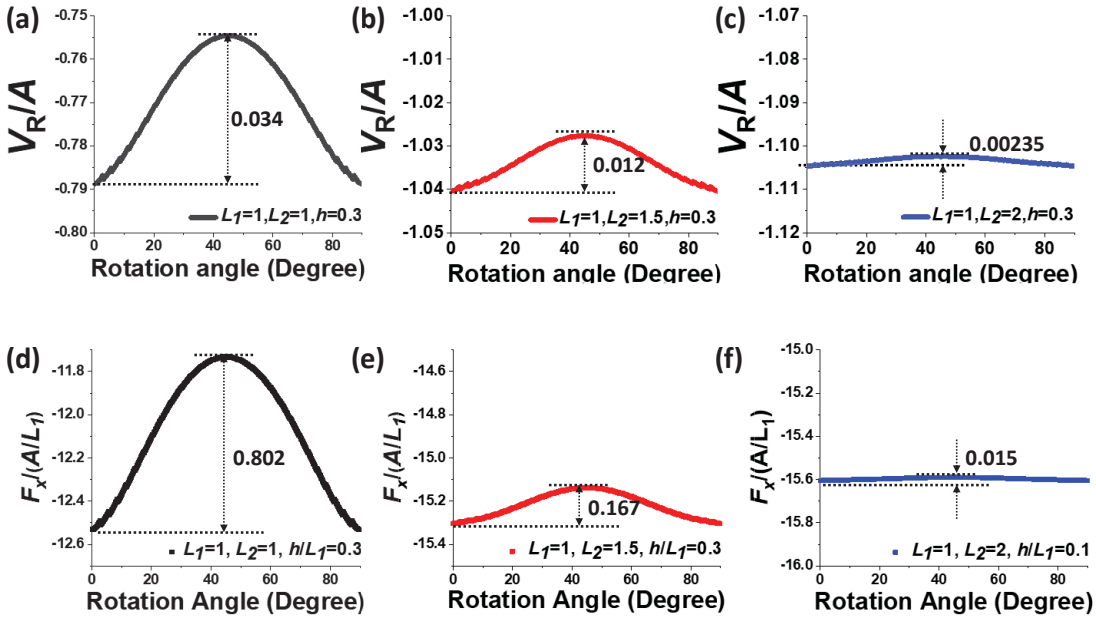

Fig. S3 Normalized van der Waals interaction potential (V/A) as a function of rotation angle (θ_x) (a) between Body 1 (L_1=1) and Body 2 (L_2=1), (b) between Body 1 (L_1=1) and Body 2 (L_2=1.5), and (c) between Body 1 (L_1=1) and Body 2 (L_2=2) at h/L_1=0.3.Normalized van der Waals interaction force ($F_x/(A/L_1)$) as a function of rotation angle (θ_x) (d) between Body 1 (L_1=1) and Body 2 (L_2=1), (e) between Body 1 (L_1=1) and Body 2 (L_2=1.5), and (f) between Body 1 (L_1=1) and Body 2 (L_2=2) at h/L_1=0.3.

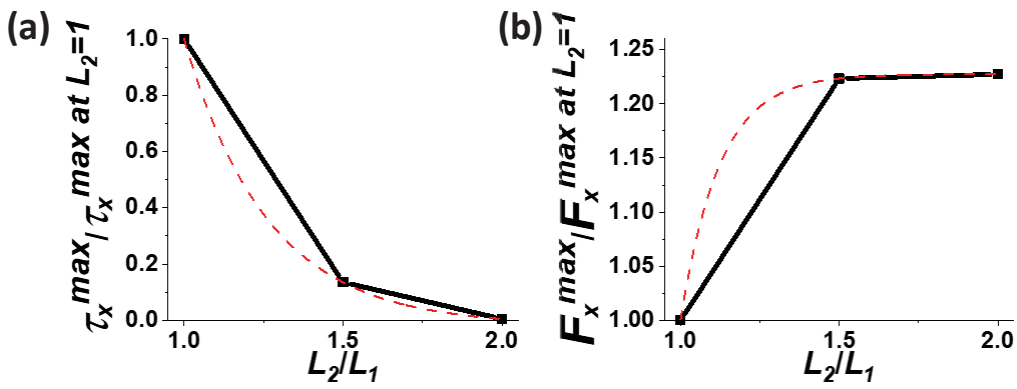

Fig. S4 (a) The ratio of the maximum normalized torque on L_2 to the maximum normalized torque of L_2=1 at normalized separation distance (h/L$_1$) =0.1 over different sizes of L_2.

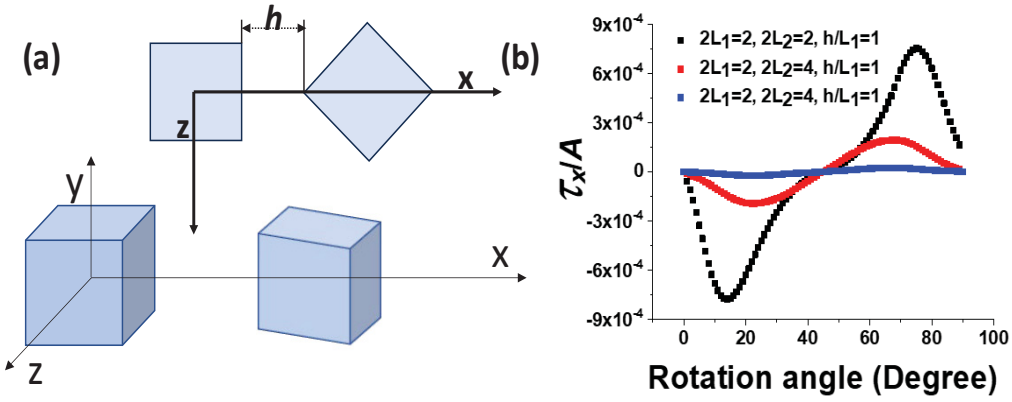

Fig. S5 (a) face-to-edge configurations, and (b) normalized van der Waals interaction torques (τ/A) as a function of rotation angle (θ_x) between cubes having smooth surfaces.

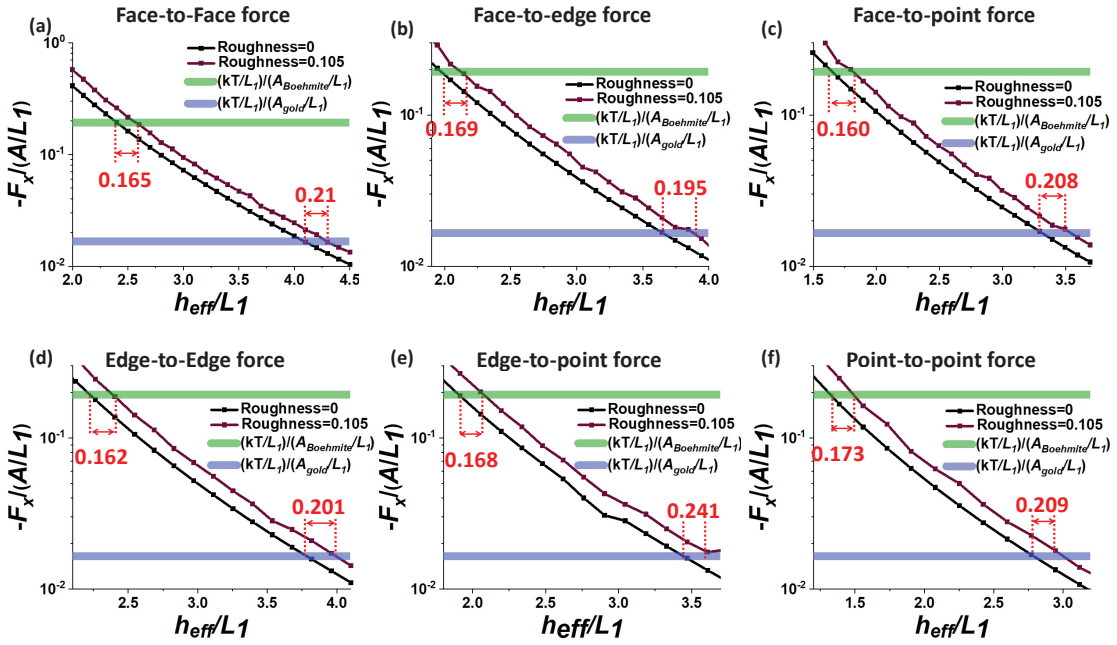

Fig. S6. Normalized van der Waals interaction force ($F/(A/L_1)$ as a function of normalized separation distance (h_{eff}/L_1) between smooth surfaces and rough surfaces (Roughness=0.105) with normalized thermal force (kT/L_1)/(A/L_1) for different configurations: (a) face-to-face, (b) Face-to-edge, (c) Face-to-point, (d) Edge-to-edge, (e) Edge-to-point, and (f) point-to-point.

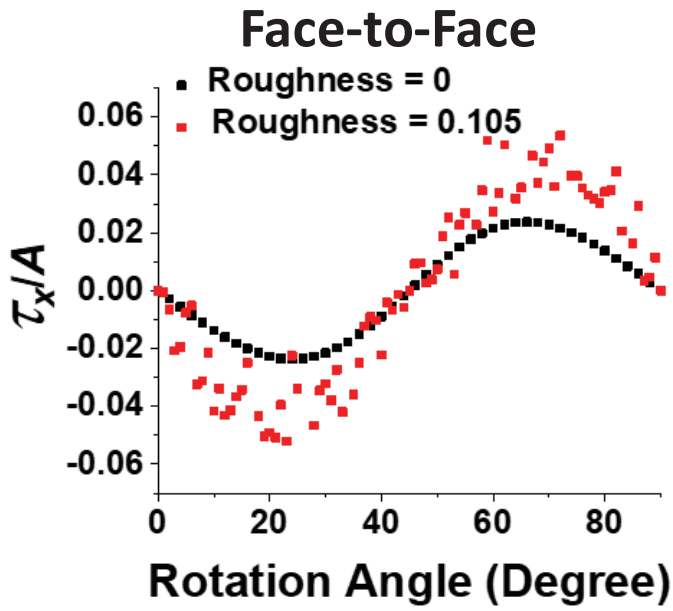

Fig. S7. Normalized van der Waals interaction torque (τ/A) as a function of rotation angle (θ_x) between smooth surfaces and rough surfaces (Roughness=0.105)

References

1. Maeda, H.; Maeda, Y., Orientation-Dependent London–van der Waals Interaction Energy between Macroscopic Bodies. *Langmuir* **2015,** *31* (26), 7251-7263.